ORIGINAL PAPER

Effect of cooling method on TiN precipitation behavior of high-titanium high-strength steel during solidification

Xue-jian Zhang[1,2] · Guang-wei Yang[3] · Yong Wan[1,2] ⓘ · Yong-hong Wen[1,2] · Chuan-sheng Tang[1,2] · Ming-qi Liu[1,2] · Li-jie Tian[1,2]

Abstract

Metallographic microscopy, scanning electron microscopy and TiN growth thermodynamic and kinetic equations were used to investigate the morphology, quantity, and size of TiN in the center of high-titanium high-strength steels under different solidification cooling rates. The results showed that TiN in the center of the experimental steels mainly existed in three forms: single, composite (Al_2O_3–TiN), and multi-particle aggregation. TiN began precipitating at around 1497 °C (solidification fraction of 0.74). From the end of melting to solidification for 180 s, the cooling rates in the center of the experimental steels for furnace cooling, air cooling, refractory mold cooling, and cast iron mold cooling tended to stabilize at 0.17, 0.93, 1.65, and 2.15 °C/s, respectively. The size of TiN in the center of the experimental steel cooled using furnace cooling was mainly concentrated in the 5–15 μm range. In contrast, the size of TiN in the center of the experimental steels cooled using air cooling, refractory mold cooling, and cast iron mold cooling were mainly concentrated in the 1–5 μm range. In addition, their density of TiN in the center of the experimental steels is significantly higher than that of the furnace-cooled experimental steel. Thermodynamic and kinetic precipitation models of TiN established predicted the growth size of TiN in a high-titanium high-strength steel when the solidification cooling rates are not below 0.93 °C/s.

Keywords High-titanium steel · Cooling method · TiN · Thermodynamics · Kinetics

1 Introduction

Engineering machinery primarily uses high-strength steel in load-bearing vehicles, lifting equipment, mining machinery, and hydraulic supports [1]. With the development of engineering machinery towards larger and lighter structures, higher demands have been placed on the toughness of high-strength steel. Currently, composite microalloying of elements, such as Nb, V, Cr, Mo, and Ni,

is used primarily to obtain high-strength steel for engineering machinery [2, 3]. In recent years, microalloying of titanium (Ti) has become an extensively studied topic in high-strength steel due to its cost advantages and the significant benefits in terms of refined grain size and dispersion strengthening compared to composite microalloying. Studies have shown that Ti combines effortlessly with N and C in steel to form small and dispersed precipitates, effectively pinning grain boundaries and hindering the growth of austenite grains to improve the strength, ductility, and anisotropy of the steel [4–6]. However, large TiN (> 10 μm) precipitates quickly form in the center of the steel during the continuous casting process for a high Ti content in the steel. These large TiN particles have triangular or quadrilateral shapes and high hardness, making them hard to dissolve and break down during subsequent heat treatment and rolling processes. Consequently, this weakens the refinement and dispersion strengthening effects of TiN, which significantly reduces

✉ Yong Wan
wanyong0729@163.com

1 Key Laboratory of Metallurgical Emission Reduction and Resources Recycling, Anhui University of Technology, Ma'anshan 243002, Anhui, China

2 School of Metallurgical Engineering, Anhui University of Technology, Ma'anshan 243002, Anhui, China

3 Baosteel Central Research Institute, Baoshan Iron and Steel Co., Ltd., Shanghai 201999, China

the strength at the center of the rolled product, and increases the cracking tendency during the hot rolling process [7–9]. Therefore, avoiding the formation of large TiN particles in the center of solidified steel is a critical issue that needs to be addressed urgently in the industrial production of Ti-microalloyed high-strength steels. Unfortunately, few reports exist on how to refine the large TiN particles in the center of high-titanium high-strength steels.

Prikryl et al. [10] found that the enrichment of Ti and N atoms at the solidification front of the molten steel could promote TiN precipitation in the later stage of continuous casting solidification. Zhan et al. [11] and Liu et al. [12] used thermodynamic calculations to explore the effects of different Ti and N contents on the TiN precipitation in microalloyed steel. They found that reducing the initial Ti and N contents could delay the start of TiN precipitation and reduce the generation of large TiN particles during solidification. Gui et al. [13] used a coupling model of Ti and N segregation and TiN precipitation and calculated that TiN grows most rapidly in the early stage of solidification and slows down gradually in the later stage. Liang et al. [14] and Li et al. [15] used Hiroki Goto's inclusion growth formula to calculate the effect of the initial N content on the growth size of TiN during the solidification process of molten steel. They found that the initial N content had a more significant effect than the initial Ti content. Most recent studies have mainly focused on establishing the correlation between the initial Ti and N contents, Ti and N segregation, and the growth size of TiN during the solidification process from the perspectives of thermodynamics and kinetics.

As mentioned above, many studies have been carried out to clarify the precipitation behavior of TiN in the solidification process. However, they ignored the possibility of the effect of other alloy components and inclusions in the steel on the growth behavior of TiN during the actual solidification process. Through laboratory experiments, this study investigated the morphology, quantity, and size changes of TiN precipitates in the center of high-titanium high-strength steels under different solidification cooling conditions. Additionally, it explored the correspondence between the temperature changes in the center of the experimental steels and the size growth of TiN. Moreover, it revealed the temperature range of large-sized TiN particles formation during actual solidification process and its internal relationship with thermal history. Furthermore, this study provided scientific guidance for the refining and regulating TiN in the center of high-titanium high-strength steel during the continuous casting process.

2 Experimental materials and methods

Four high-titanium high-strength steels were smelted at 1560 °C. Their chemical compositions are listed in Table 1. After the steels were completely melted, they were cooled to room temperature using four different cooling methods. Four cooling methods, including furnace cooling, air cooling, pouring into a 1100 °C refractory mold, and pouring into a 1100 °C cast iron mold, were used to cool the steels Nos. 1–4, respectively. The solidification and cooling processes of the four steels were continuously monitored for temperature changes in the central region. The schematic diagram for measuring temperature is depicted in Fig. 1.

During temperature measurement, the thermocouple is securely fixed and connected to the temperature measuring instrument via its head. The tail of the thermocouple is left with sufficient length to ensure smooth and accurate insertion into the molten steels core for precise temperature readings. After the steels were completely cooled, samples (ϕ16 mm × 16 mm) were taken from the temperature measurement position in the center of the steels. The cross-section of the thermocouple measuring point was ground, polished, and etched with a 4 vol.% nitric acid solution. The typical morphology and composition of TiN on the etched surface of each sample were observed and analyzed using a scanning electron microscope (JEM-6510). The etched surfaces were continuously observed and photographed using a metallurgical microscope (UCMOS03100KPA). Photoshop software was used to statistically analyze and measure the quantity and size of TiN within each field of view to calculate the TiN density in different size ranges. TiN density is defined as the total number of TiN divided by the total area. The equilibrium concentration product $\lg K_{\mathrm{TiN}}$, actual concentration product $\lg Q_{\mathrm{TiN}}$, onset precipitation temperature, and growth size in the solid–liquid two-phase and solid phase regions of TiN were calculated using the nucleation and growth kinetic equations of TiN precipitation under different nucleation mechanisms in the solid–liquid two-phase and the austenite solid phase regions.

3 Experimental results and analysis

3.1 Temperature variation in center of experimental steels under different cooling methods

The temperature variation curves in the experimental steels core with solidification time under different cooling methods are shown in Fig. 2. As indicated in Fig. 2a, steel

Table 1 Chemical composition of experimental steels (wt.%)

No.	C	Si	Mn	P	S	Al	Ti	TO	N
1	0.076	0.065	1.649	0.0118	0.0023	0.051	0.10	0.0007	0.0120
2	0.080	0.133	1.632	0.0132	0.0026	0.059	0.11	0.0011	0.0115
3	0.072	0.120	1.643	0.0147	0.0029	0.063	0.12	0.0009	0.0112
4	0.078	0.104	1.651	0.0121	0.0021	0.057	0.11	0.0014	0.0124
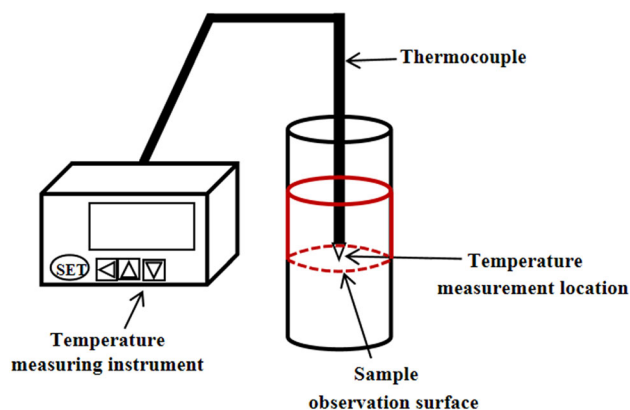

Fig. 1 Schematic diagram of temperature measurement

No. 1, employing an in-furnace cooling process, exhibited a nearly constant cooling rate of 0.17 °C/s during its descent from 1560 °C to room temperature, as specified by the cooling program of the melting furnace. However, steels Nos. 2–4 exhibited a relatively faster temperature decrease at the early stage of solidification in the central region. The temperature decrease in the center gradually slowed down as the steels continued to cool. As seen in Fig. 2b, the cooling rates of the center temperature for steels Nos. 1–4

tended to be constant from the end of melting to 180 s of solidification and were 0.17, 0.93, 1.65, and 2.15 °C/s, respectively. The mean temperatures of steels Nos. 1–4 dropped to 1530, 1411, 1216, and 1091 °C at 180 s of solidification, respectively.

3.2 Metallographic structures and TiN morphologies in center of experimental steels under different cooling methods

The microstructure and TiN morphology in the experimental steels core under different cooling methods are shown in Fig. 3. As shown in Fig. 3a, the microstructure of steel No. 1 cooled in the furnace consisted mainly of coarse-grained polygonal ferrite and pearlite with large polygonal (such as triangles and quadrilaterals) TiN particles with sharp edges in the matrix, which have a size of 17.08 μm. As seen in Fig. 3b, the polygonal ferrite and pearlite size in steel No. 2 decreased significantly when the solidification cooling method was changed to air cooling. Furthermore, the pearlite largely disappeared in steels No. 3 and No. 4, and more granular bainite appeared when the solidification cooling method was changed to refractory mold cooling and cast iron mold cooling, as seen in Fig. 3c, d. The main reasons for this phenomenon may be
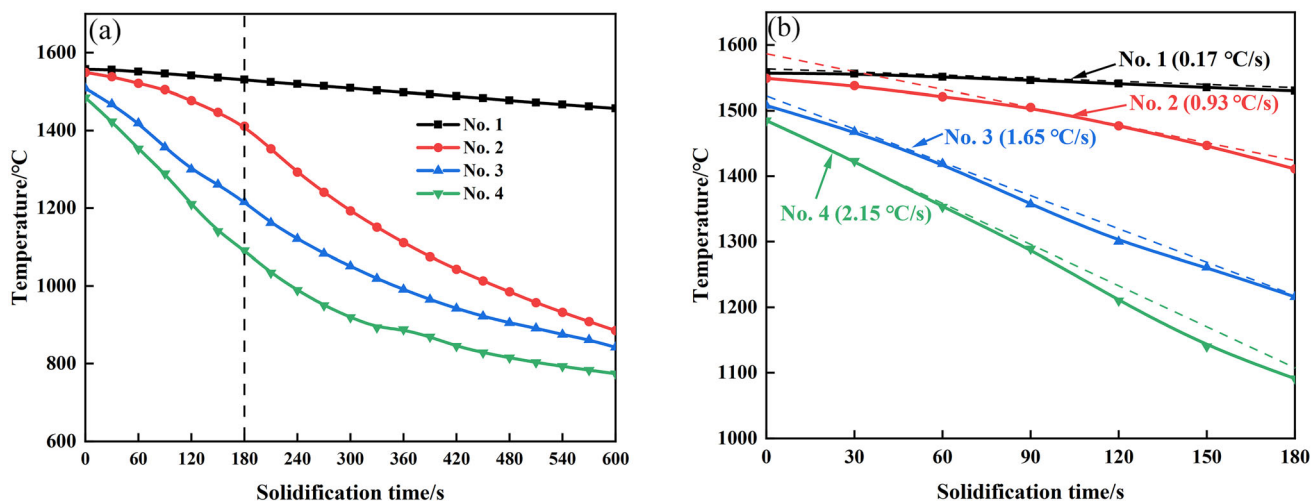
Fig. 2 Temperature change curve of different experimental steels core with time. **a** First 600 s after casting; **b** first 180 s after casting

twofold. On the one hand, the high titanium content in the steel makes it easy to form carbonitrides with carbon and nitrogen, effectively hindering carbon diffusion and the precipitation of carbides. On the other hand, the continuously increasing cooling rate further reduces the diffusion rate of alloying elements such as Ti and C during solidification, hampering the austenite-to-ferrite transformation and inhibiting pearlite formation. Therefore, as the solidification cooling method changed from furnace cooling → air cooling → refractory mold cooling → cast iron mold cooling, with gradually increasing cooling intensity, the grain size of ferrite in the experimental steels gradually decreased, and pearlite was gradually refined and transformed into granular bainite [16]. Additionally, the precipitation morphology of TiN in the matrix showed that the number of TiN particles in the experimental steels significantly increased, but their size continuously decreased as the solidification cooling intensity increased. This is because increasing the cooling rates at lower cooling intensities will cause a greater undercooling and higher oversaturation of microalloying elements Ti and N, increasing the driving force for TiN nucleation and enabling its precipitation [17–19]. Additionally, increasing the cooling rates will rapidly reduce the diffusion rate of Ti and N atoms in the solidification process and significantly shorten the growth time of TiN particles so that they cannot grow larger, significantly decreasing their size [20].

The microstructure and TiN morphology in the experimental steels core with different cooling methods were investigated. Scanning electron microscopy revealed many individual TiN particles, Al_2O_3–TiN composite inclusions with Al_2O_3 as the core, and multiple agglomerated TiN particles in the experimental steels core, as seen in Figs. 4 and 5. The size of the Al_2O_3 core in the Al_2O_3–TiN composite inclusions ranged from 1 to 2 μm. Al_2O_3 and TiN belong to the hexagonal and the face-centered cubic crystal systems, respectively. The degree of mismatch between them can be calculated using Eq. (1),

$$\delta_{(hkl)_n}^{(hkl)_s} = \sum_{i=1}^{3} \left[\frac{\left| d_{[uvw]_s}^i \cos\theta - d_{[uvw]_n}^i \right|}{d_{[uvw]_n}^i} \right] \times \frac{1}{3} \times 100\% \qquad (1)$$

where s and n represent the substrate and nucleating phase, respectively [21]. (hkl), [uvw], and $d_{[uvw]}$ represent a low-index crystal plane in the substrate or nucleating phase, a low-index direction on the (hkl) crystal plane, and the interatomic spacing along the [uvw] direction, respectively. θ represents the angle between $[uvw]_s$ and $[uvw]_n$. The mismatch between Al_2O_3 and TiN calculated using Eq. (1) and the data in Tables 2 and 3 was 10.91%. Generally, when the mismatch between the two phases is less than 12%, the first precipitated compound phase can act as a non-spontaneous nucleus to promote nucleation. The high-melting-point Al_2O_3 preferentially precipitates and can
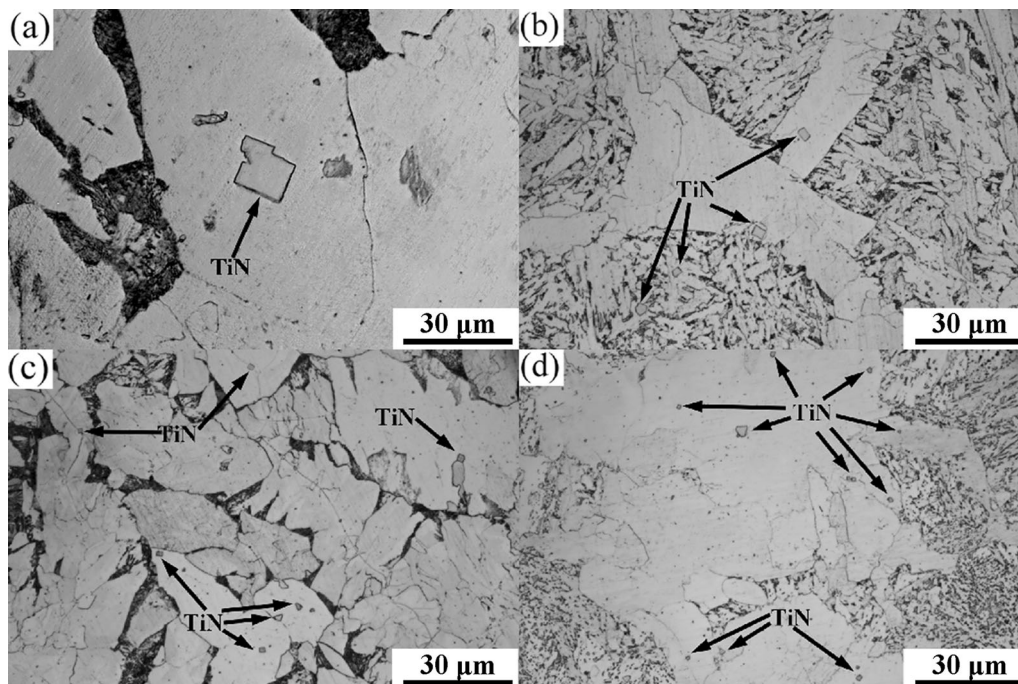

Fig. 3 Metallographic structure and TiN morphology in experimental steels core under different cooling methods. **a** No. 1; **b** No. 2; **c** No. 3; **d** No. 4
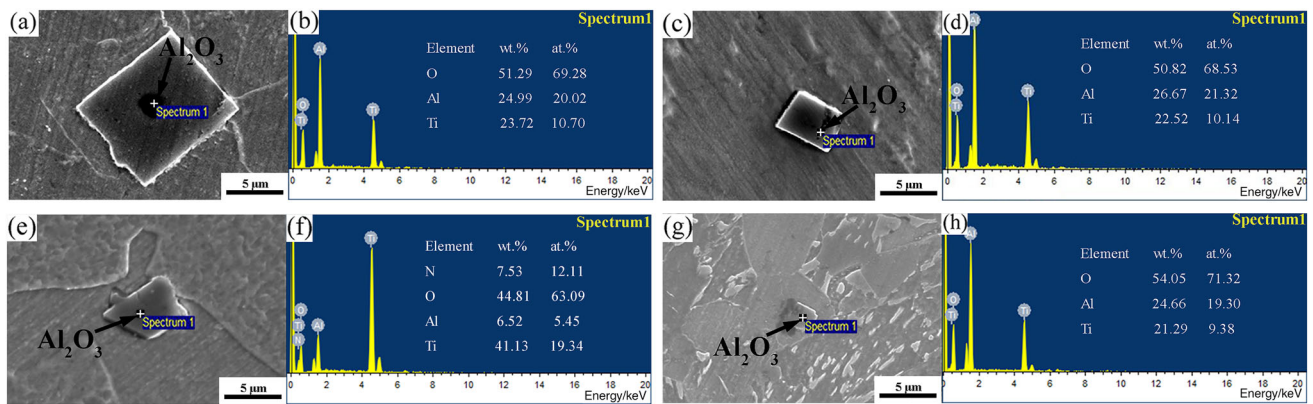
Fig. 4 Morphology and energy spectrum analysis results of Al_2O_3–TiN composite inclusion. **a**, **b** No. 1; **c**, **d** No. 2; **e**, **f** No. 3; **g**, **h** No. 4
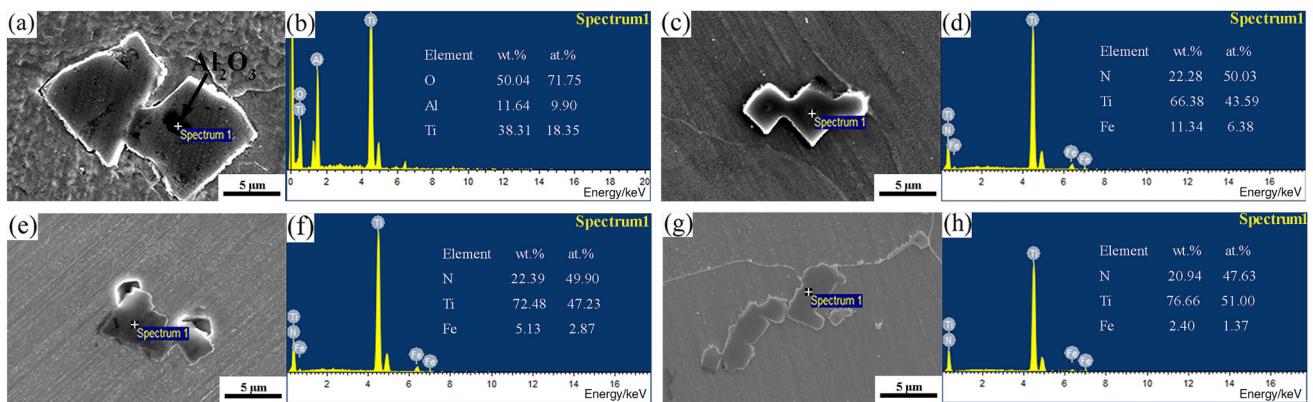

Fig. 5 Morphology and energy spectrum analysis results of aggregated TiN inclusions. **a**, **b** No. 1; **c**, **d** No. 2; **e**, **f** No. 3; **g**, **h** No. 4

serve as a heterogeneous nucleating core for TiN due to its low degree of mismatch with TiN. Additionally, titanium (Ti) segregation during the solidification process results in significantly higher Ti concentrations at the solidification front than the critical Ti concentration required for TiN heterogeneous nucleation [22]. Consequently, TiN readily nucleates around Al_2O_3 cores in large quantities during solidification. Moreover, the agglomeration of the TiN particles may be due to the proximity of some individual TiN particles, which spontaneously form cavities and are attracted to each other under the infzzluence of cavity-bridging forces [23].

3.3 Quantities, sizes and precipitation locations of TiN (≥ 1 μm) in center of experimental steels under different cooling methods

The statistical results of the quantity, size, and precipitation location of TiN (≥ 1 μm) in the central region of experimental steels under different cooling methods are shown in Fig. 6. As shown in Fig. 6a, the size of TiN particles in core of steel No. 1 was mainly concentrated between 5–15 μm, with a higher density between 8–12 μm when the solidification cooling method was furnace cooling. As the solidification cooling method changed from furnace cooling → air cooling → refractory mold cooling → cast iron mold cooling, the total density of TiN precipitated in

Table 2 Crystallographic parameters of Al_2O_3 and TiN (Å)

Nucleating phase	Lattice structure	Lattice parameter (25 °C)		Lattice parameter (1600 °C)	
		a_0	c_0	a_{01}	c_{01}
Al_2O_3	Hexagonal crystal system	4.758	12.991	4.822	–
TiN	Face-centered hexagonal crystal system	4.241	–	4.305	–

Table 3 Calculation results of mismatch degree between (0001) surface of Al_2O_3 and (110) surface of TiN

Matching surface	$[uvw]_{Al_2O_3}$	$[uvw]_{TiN}$	$d_{[uvw]_{Al_2O_3}}$	$d_{[uvw]_{TiN}}$	$\theta/(°)$	$\delta/\%$
	[1210]	[110]	4.822	6.088	0	
$(0001)Al_2O_3//(110)TiN$	[2110]	[112]	4.822	5.272	5.3	10.91
	[1010]	[001]	8.352	8.610	0	

each experimental steels core sharply increased. The size of the TiN particles was mainly concentrated between 1–5 μm, and a few of them were larger than 8 μm. As shown in Fig. 6b, the maximum size of TiN in each experimental steels core decreased from 17.81 μm → 8.31 μm →6.58 μm → 5.33 μm when the solidification cooling method changed from furnace cooling → air cooling → refractory mold cooling → cast iron mold cooling, respectively. Additionally, the average size decreased from 9.86 μm → 4.34 μm → 2.93 μm → 2.79 μm when the solidification cooling method changed from furnace cooling → air cooling → refractory mold cooling → cast iron mold cooling, respectively. As seen in Fig. 6c, $TiN_{grain\ boundary}$ had a slightly larger average size in steels Nos. 1–4 than $TiN_{grain\ interior}$. However, $TiN_{grain\ boundary}$ had a significantly lesser number than $TiN_{grain\ interior}$. This is primarily because the atoms on the grain boundary are disordered and have higher energy and more vacancies compared with the grain interior, which is more conducive to the diffusion of Ti and N atoms. Additionally, TiN particles nucleate earlier and grow faster on the grain boundary since TiN have much lower critical nucleation energy on the grain boundary than in the grain interior [24]. Moreover, since the grain interior had a much larger total area than the grain boundary, Ti and N atoms had more space to diffuse, aggregate, or continuously diffuse to some micro-inclusions or solidification defects to form TiN nucleation sites in the grain interior. Therefore, the TiN precipitates had a significantly greater number in the grain interior than on the grain boundary. The ratio of $TiN_{grain\ boundary}$ to $TiN_{grain\ interior}$ in each experimental steels core changed from 0.29 → 0.24 → 0.18 → 0.16 when the solidification cooling method changed from furnace cooling → air cooling → refractory mold cooling → cast iron mold cooling, respectively. This is primarily because the increase in solidification cooling rate effectively reduces the migration rate of Ti and N atoms in the matrix, significantly inhibiting their diffusion and aggregation to long-distance grain boundaries [25]. Additionally, Ti and N atoms are highly supersaturated in the matrix, further intensifying the nucleation tendency of TiN in the grain interior.

4 Thermodynamic and kinetic analysis of TiN precipitation during solidification and solid-state cooling processes

4.1 Onset precipitation temperature of TiN at solidification front

The solubility of Ti and N atoms in the liquid phase was higher than that in the solid phase when molten steel solidified, gradually enriching and segregating Ti and N atoms at the solidification front. TiN started to precipitate when lgQ_{TiN} of TiN exceeded its lgK_{TiN}. lgK_{TiN} and lgQ_{TiN} can be calculated using Eqs. (2) and (3) in Table 4. In Eqs. (2) and (3), T represents the temperature at the solidification front (in °C). f_{Ti} and f_N represent the dimensionless activity coefficients of Ti and N when the solidification front temperature is T, respectively. $w[Ti]$ and $w[N]$ represent the actual concentrations (in %) of Ti and N at the solidification front, respectively. T can be determined using Eqs. (4) and (5) in Table 4 and the ΔT values in Table 5 [26, 27]. f_{Ti} and f_N can be calculated using Eqs. (5)–(8) in Table 4 and the data in Table 6 [28]. T_0 represents the melting point of pure iron (1538 °C). $T_{L/S}$ (T_L and T_S) represent the temperatures (in °C) of the liquidus and solidus lines, respectively. g represents the dimensionless solidification fraction. e_{Ti}^i and e_N^i represent the interaction coefficients between Ti and N and the element i, respectively [29]. $w[j]$ represents the mass percentage of element j in steel.

The Ohnaka equation, given as Eq. (10) in Table 7, can be used to calculate $w[Ti]$ and $w[N]$ at the solidification front. Equations (11)–(13) given in Table 7 can be used to calculate the inverse diffusion coefficient β, the local solidification time τ, and the secondary dendrite arm spacing L, respectively [30]. In Eqs. (10)–(13), $w[i]_0$ represents the initial concentration (in %) of element i (Ti or N). k represents the equilibrium partition coefficient of Ti or N between liquid and solid phases. D_i represents the diffusion coefficient (in cm^2/s) of Ti or N, where R represents the ideal gas constant, and its calculation formula is shown in Table 8. C_R and $w[C]$ represent the cooling rate (in °C/s) and the carbon content in the steel (in %), respectively.
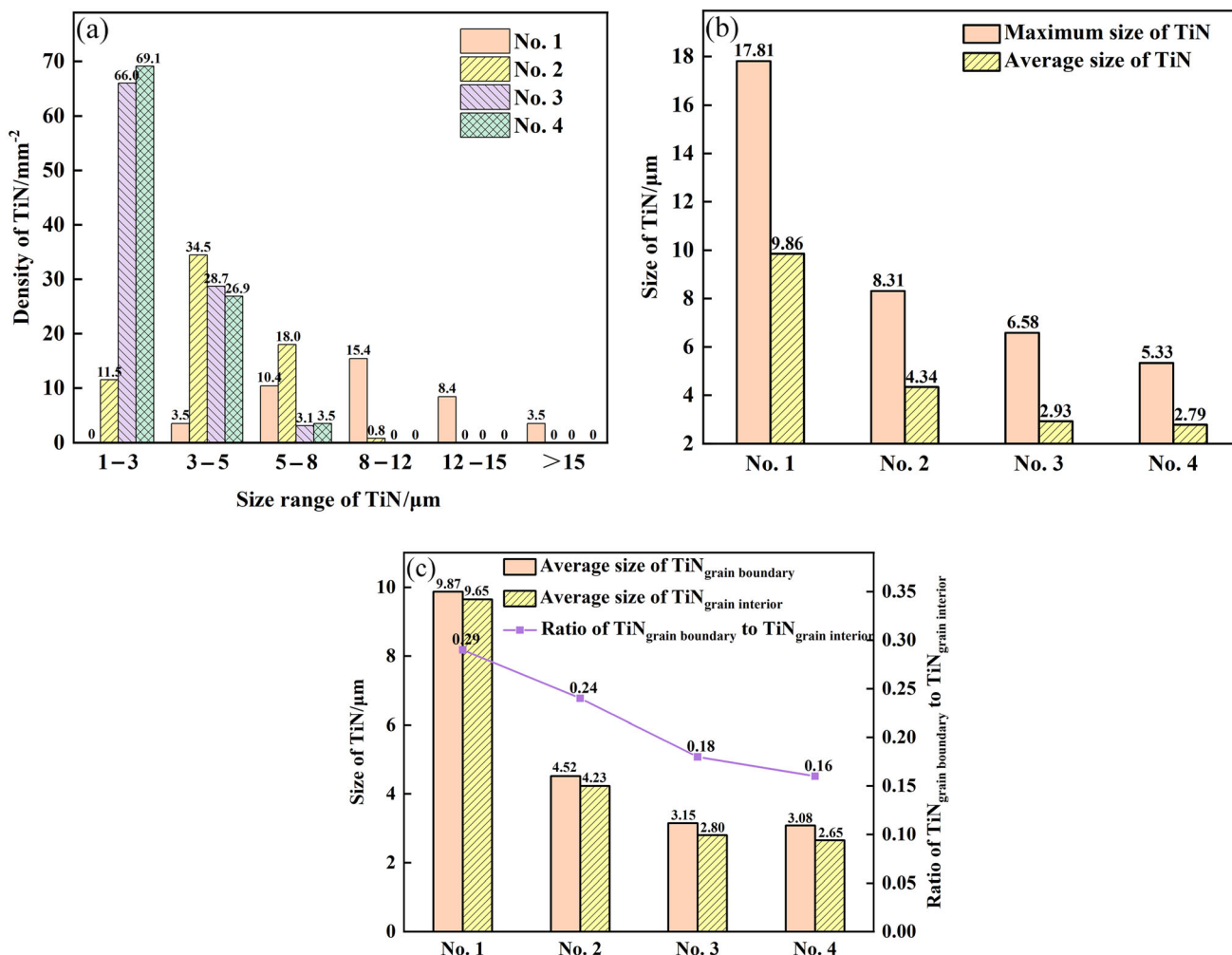
Fig. 6 Statistical results of TiN density, maximum size, average size, and precipitation position in experimental steels core under different cooling methods. **a** Density of TiN; **b** maximum and average sizes of TiN; **c** average size of $TiN_{grain\ boundary}$ and $TiN_{grain\ interior}$, and ratio between them

Table 4 Equations required for calculating $lg K_{TiN}$ and $lg Q_{TiN}$

$\lg K_{TiN} = 5.64 - 15,218/T$	(2)	$\lg f_{Ti(1600)} = \sum e_{Ti}^i w[j]$	(6)
$\lg Q_{TiN} = \lg(f_{Ti} \cdot f_N \cdot w[Ti] \cdot w[N])$	(3)	$\lg f_{N(1600)} = \sum e_N^i w[j]$	(7)
$T = T_0 - \frac{T_0 - T_L}{1 - g\frac{T_L - T_S}{T_0 - T_S}}$	(4)	$\lg f_{Ti} = (2557/T - 0.365)\lg f_{Ti(1600)}$	(8)
$T_{L/S} = 1538 - \sum \Delta T \cdot w[j]$	(5)	$\lg f_N = (3280/T - 0.75)\lg f_{N(1600)}$	(9)

Table 5 ΔT value required for calculating liquidus and solidus

Element	C	Si	Mn	P	S	Al	Ti	TO	N
Liquidus ΔT	65	8	5	30	25	3	20	80	90
Solidus ΔT	175	20	30	280	575	7.5	40	160	–

Table 6 e_{Ti}^i and e_N^i in molten steel at 1600 °C

Element	C	Si	Mn	P	S	Al	Ti	O	N
Ti	− 0.19	2.1	− 0.43	− 0.0064	− 0.11	0.0037	0.013	− 1.8	− 2.03
N	0.13	0.047	− 0.02	0.045	0.007	− 0.028	− 0.53	0.05	0

Table 7 Equations required for calculating $w[Ti]$ and $w[N]$

$w[i] = w[i]_0 \cdot [1 - (1 - \beta k/(1+\beta))g]^{(k-1)/(1-\beta k/(1+\beta))}$	(10)		$\tau = (T_L - T_S)/C_R$	(12)
$\beta = 4D_i \cdot \tau/L^2$	(11)		$L = (169.1 - 720.9 \cdot w[C]) \cdot C_R^{-0.4935}$	(13)

The relationship between $\lg K_{TiN}$ and $\lg Q_{TiN}$ of TiN at the solidification front for steels Nos. 1–4 with decreasing temperature is shown in Fig. 7 based on the calculation formulas and data in Tables 4–8, the chemical composition of the steels as shown in Table 1, and the average cooling rates of the steels within the first 180 s after casting under different cooling methods (Fig. 2b). The different solidification cooling methods had little influence on the starting precipitation temperature of TiN in each experimental steel. Additionally, TiN in the steel began to precipitate at around 1497 °C (solidification fraction of 0.74), i.e., in the solid–liquid two-phase region.

4.2 Growth behavior of TiN during solidification and solid-phase cooling processes

4.2.1 Growth model of TiN during solidification process

Furthermore, Ti is more likely to accumulate at the solidification front since N has a higher diffusion coefficient than Ti in the steel melt. Therefore, the diffusion of N in the steel melt controls the TiN growth during the solidification process [15]. The kinetic model for TiN growth during the solidification process is expressed in Eq. (14) [13]. In Eq. (14), r_0, M_s, ρ_m, M_N, and ρ_s represent the radius of TiN (in μm), the molar mass of TiN (62 g/mol), the density of the steel melt (7.07 g/cm³), the molar mass of nitrogen (14 g/mol), and the density of TiN (5.43 g/cm³), respectively. $w[N]_e$ represents the equilibrium concentration of N during TiN precipitation (in %). τ_0 represents the time interval (in s) from the start of TiN precipitation to the complete solidification of the steel melt.

Table 8 k and D_i of Ti and N

Element	k	$D_i/(cm^2 \ s^{-1})$
Ti	0.33	$0.15e^{[-250,956/(RT)]}$
N	0.48	$0.91e^{[-168,490/(RT)]}$

$$r_0 = 10^4 \sqrt{\frac{M_s \rho_m D_N \cdot [w[N] - w[N]_e] \cdot \tau_0}{50 M_N \rho_s}} \quad (14)$$

4.2.2 Growth model of TiN during solid-phase cooling process

Further cooling after the complete solidification of molten steel would lead to Ostwald ripening and TiN growth, driven by the interfacial energy between TiN and the matrix. The diffusion of Ti and N atoms in the matrix primarily influences this process. The theoretical formula for the Ostwald ripening of TiN in austenite, the coarsening rate m, and the interfacial energy between TiN and austenite σ can be expressed as Eqs. (15)–(19) in Table 9 [31, 32]. Equations (20) and (21) can be used to calculate the equilibrium solubility of Ti and N in austenite and the consumption of Ti and N atoms during the growth process
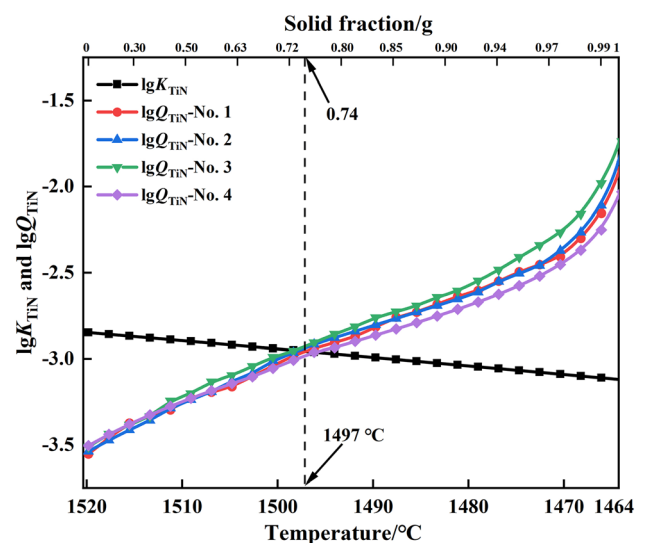

Fig. 7 Values of $\lg K_{TiN}$ and $\lg Q_{TiN}$ at different temperatures during solidification process

Table 9 Calculation equations of TiN growth in solid phase

$r_1^3 = r_0^3 + m^3 t$	(15)	$\sigma = (5.8458 - 2.6342 \times 10^{-3} T) f(\delta)$	(19)
$m = \left(\dfrac{8 \sigma V_P^2 D_i C_{i-eq}}{9 V_B C_P R T} \right)^{1/3}$	(16)	$\lg(x(i) \cdot x(j))_{\gamma - Fe} = 0.32 - 8000/T$	(20)
$\delta = \left| \dfrac{a_C - a_\gamma}{a_C} \right|$	(17)	$\dfrac{x(i) - x(i)_{eq}}{x(j) - x(j)_{eq}} = \dfrac{M_i}{M_j}$	(21)
$f(\delta) = \delta \left[\dfrac{2}{1 + \frac{1}{4\delta^2}} - \ln(2\delta) \right]$	(18)	$C_{i-eq} = \dfrac{x(i)_{eq}/M_i}{(100 - x(i)_{eq})/M_{Fe} + x(i)_{eq}/M_i}$	(22)

of TiN, respectively [32, 33]. As calculated using Eq. (22) and the relevant parameters in Table 9, $D_{Ti}C_{Ti-eq}$ was always less than $D_N C_{N-eq}$ during the cooling process of austenite, indicating that Ti diffusion mainly affected the TiN growth in austenite. In Eqs. (15)–(22), r_1 and r_0 represent the size of TiN (in μm) at time t and initial time, respectively. V_P and V_B represent the molar volumes of TiN (1.18186 m³/mol) and steel matrix (7.52675 m³/mol), respectively. C_{i-eq} and C_P are the equilibrium mole fractions of the controlling element i in the steel matrix and the precipitate phase, respectively. δ represents the mismatch between TiN and austenite. a_C and a_γ represent the lattice constants of TiN (0.4241 nm) and austenite (0.3681 nm), respectively. $x(i)$ and $x(j)$ represent the contents of i and j in steel, respectively. $x(i)_{eq}$ and $x(j)_{eq}$ represent the equilibrium contents of i and j in austenite, respectively. M_i and M_j represent the atomic weights of i and j, respectively. In Table 9, i and j represent Ti and N, respectively.

4.2.3 Size changes of TiN during solidification and solid-state cooling processes

The size changes of TiN during solidification and solid-state cooling processes for steels Nos. 1–4 were calculated based on Eqs. (14)–(22) and relevant parameters, as shown in Fig. 8. TiN nucleated and grew in all steels when the temperature of the steel substrate was below 1497 °C (solidification fraction of 0.74), and the temperature range for rapid TiN growth was 1464–1497 °C (corresponding to a solidification fraction of 0.740–1.000). TiN in steels Nos. 1–4 could grow to 20.07, 8.72, 6.79, and 5.54 μm, respectively, when the temperature decreased from 1497 to 1464 °C. Furthermore, the already precipitated TiN in steels Nos. 1–4 could grow by 30 nm, with a nanoscale size that is much smaller than their growth size in the solid–liquid two-phase region when the temperature dropped from 1464 to 900 °C (austenite region). Therefore, large-sized TiN (≥ 1 μm) were formed in the solid–liquid two-phase region of steels Nos. 1–4 , and the cooling rate in this region mainly influenced the growth size of TiN.

The nucleation, growth, and aggregation processes of TiN in the solid–liquid two-phase region of steels Nos. 1–4 under various cooling methods are shown in Fig. 9. Ti and N atoms were expelled from the dendritic tips and enriched in the interdendritic melt during solidification of the steels since their equilibrium distribution coefficients were significantly less than one in the solid and liquid phases (Table 8), resulting in a higher solute concentration of Ti and N atoms in the interdendritic region compared to the dendritic interior. The concentrations of Ti and N atoms accumulated in the interdendritic melt gradually increased as the temperature decreased and the dendrites continued to grow. Subsequently, TiN began to precipitate when their concentrations exceeded the critical levels required for TiN nucleation. In contrast, the driving force for TiN nucleation and growth was relatively weaker in the dendritic interior, where the Ti and N concentrations were lower. Consequently, TiN nucleation lagged, and its growth proceeded slowly within the dendritic interior. The solidification interface of the steels transitioned from coarse dendrites (or equiaxed grains) to progressively finer dendrites as the solidification cooling rates varied from furnace
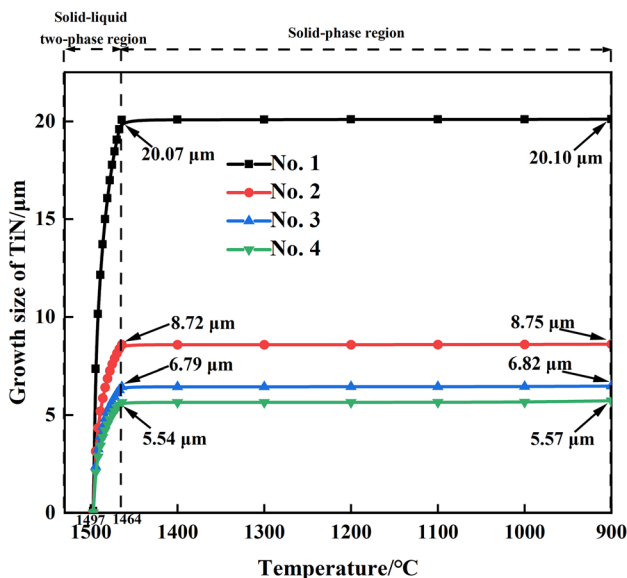

Fig. 8 Relationship between growth size of TiN and temperature during solidification and solid-state cooling processes
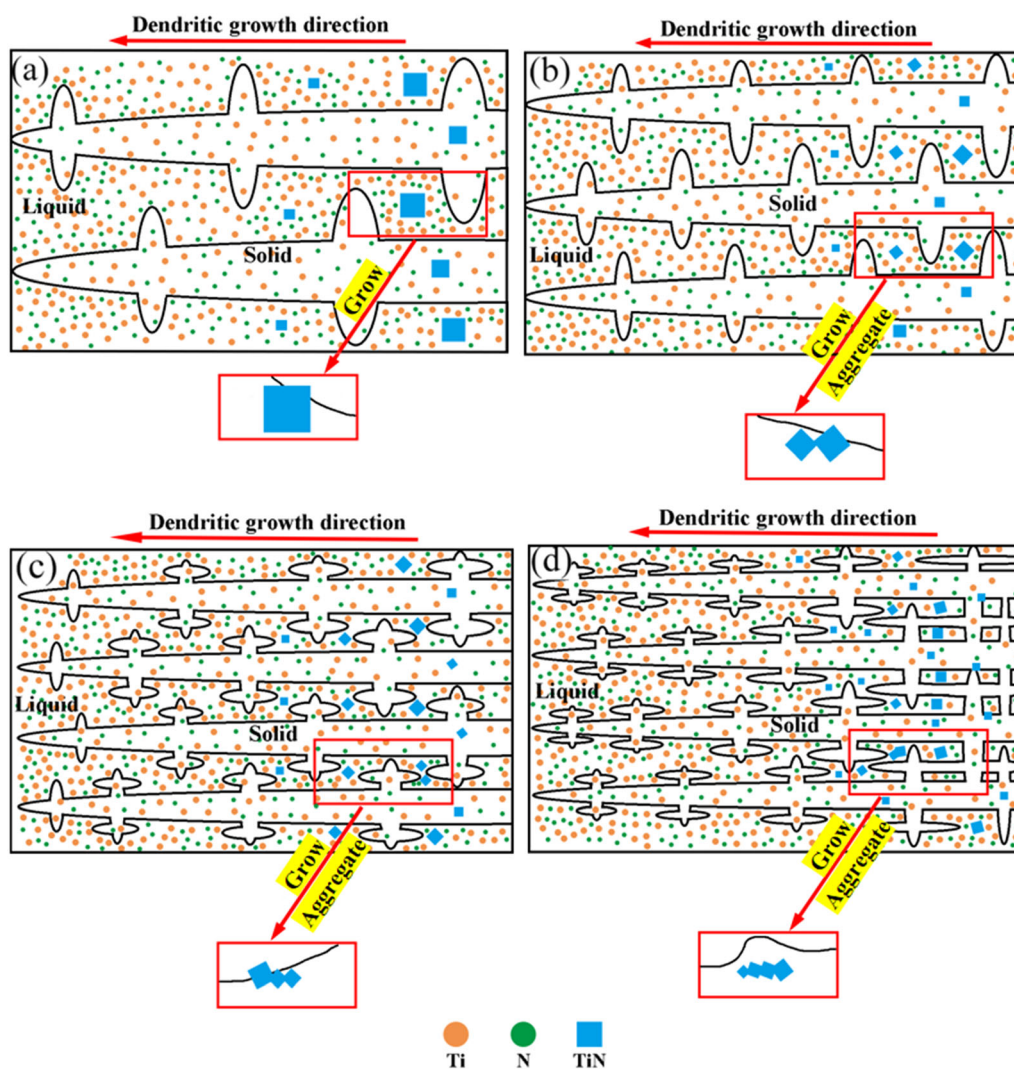
Fig. 9 Growth and aggregation schematic of TiN in solid–liquid two-phase region under different cooling methods. **a** No. 1; **b** No. 2; **c** No. 3; **d** No. 4

cooling → air cooling → refractory mold cooling → cast iron mold cooling. The primary and secondary dendrite arms of the fine dendrites were more prone to bridging with other dendrite arms since they were more developed and grew faster than those of the coarse dendrites, forming more closed liquid regions. Moreover, these regions impede the interdendritic flow and mixing of the melt, severely hindering the migration and enrichment of Ti and N atoms between dendrites [34]. Consequently, the growth of fine dendrites facilitated the formation of more regions with low Ti and N concentrations than the coarse dendrites, creating favorable conditions for TiN nucleation and refinement. The fine dendrite arms were continuously dissolved while the coarse dendrite arms thickened and evolved into grain boundaries during dendrite growth due to solute concentration gradients. Simultaneously, TiN particles nucleated within the interdendritic space grew

larger and approached the grain boundaries as the dendrites grew. Therefore, the high cooling intensity of steel No. 4 resulted in a larger quantity and smaller size of agglomerated TiN particles near the grain boundaries compared to the low cooling intensity of steel No. 1.

The comparison of the experimental results of TiN growth size in steels different solidification cooling methods with the thermodynamic and kinetic calculation results is shown in Fig. 10. The experimental results of TiN growth size in steels Nos. 1–4 were smaller than the calculated results. Compared with the calculated results, the experimental results of TiN growth size in steel No. 1 with a 0.17 °C/s solidification cooling rate showed a significant deviation of 12.9% $\left(\dfrac{\text{Calculation result - Experimental result}}{\text{Experimental result}} \right)$. The experimental results of TiN precipitation size in steels Nos. 2–4 with relatively high solidification cooling rates
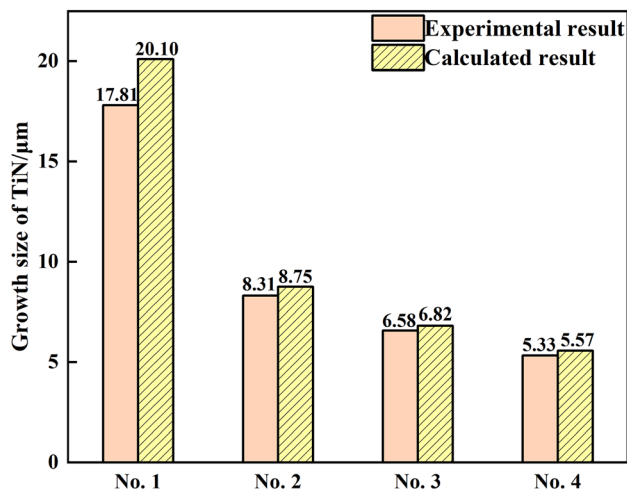
Fig. 10 Comparison between experimental and calculated results of TiN grain growth size in various steels under different solidification cooling methods

showed a slight deviation between 3.6% and 5.3% compared with steels the calculated results. Compared with steels Nos. 2–4, the significant difference between the experimental and the calculated results of the TiN growth size in steel No. 1 may be primarily attributed to the more significant hindrance of diffusion and aggregation of Ti and N atoms at the solidification front due to other solute atoms and inclusions in the steel. Therefore, the TiN precipitation thermodynamic and kinetic model established in this study has good accuracy and practicality in predicting the growth size of TiN in high-titanium high-strength steel matrices when the solidification cooling rate is not below 0.93 °C/s.

5 Conclusions

1. From the end of melting to solidification for 180 s, the experimental steel core cooling rates under furnace cooling, air cooling, refractory material mold cooling, and cast iron mold cooling tended to stabilize at 0.17, 0.93, 1.65, and 2.15 °C/s, respectively. Additionally, their core temperatures dropped to 1530, 1411, 1216, and 1091 °C, respectively, at 180 s of solidification.
2. TiN in steels Nos. 1–4 mainly existed in three forms after solidification cooling: single, composite (Al_2O_3–TiN), and multi-particle aggregation types. The size of TiN in the center of the experimental steel under furnace cooling was mainly concentrated in the 5–15 μm range, and the highest precipitation density was within 8–12 μm. In contrast, the density of TiN in the center of the experimental steels under air cooling, refractory mold cooling, and cast iron mold cooling was significantly higher. The size of TiN particles was mainly concentrated in the 1–5 μm range.

3. The maximum size of TiN in the core of the experimental steels decreased from 17.81 μm →8.31 μm →6.58 μm →5.33 μm when the solidification cooling method changed from furnace cooling → air cooling → refractory mold cooling → cast iron mold cooling, respectively. Additionally, their average size decreased from 9.86 μm → 4.34 μm → 2.93 μm → 2.79 μm.
4. The solidification cooling method had little effect on the starting precipitation temperature of TiN in high-titanium high-strength steel. The starting precipitation temperature of TiN in the steel was around 1497 °C (solid fraction of 0.74). The TiN precipitation thermodynamic and kinetic models established in this study had good accuracy and practicality in predicting the growth size of TiN in the matrix of high-titanium high-strength steel when the solidification cooling rates were greater than 0.93 °C/s.

Declarations

References

[1] R. Geng, J. Li, C. Shi, J. Zhi, B. Lu, Mater. Sci. Eng. A 840 (2022) 142919. https://doi.org/10.1016/j.msea.2022.142919.

[2] J.H. Jang, C.H. Lee, Y.U. Heo, D.W. Suh, Acta Mater. 60 (2012) 208–217. https://doi.org/10.1016/j.actamat.2011.09.051.

[3] X.L. Li, S.D. Wang, Acta Metall. Sin. 51 (2015) 417–424. https://doi.org/10.11900/0412.1961.2014.00582.

[4] H. Ohta, H. Suito, ISIJ Int. 47 (2007) 197–206. https://doi.org/10.2355/isijinternational.47.197.

[5] S. Chen, L. Li, Z. Peng, X. Huo, H. Sun, J. Mater. Res. Technol. 10 (2021) 580–593. https://doi.org/10.1016/j.jmrt.2020.12.048.

[6] L. Xing, J. Guo, X. Li, Z. Zhang, M. Wang, Y. Bao, F. Zeng, B. Chen, Mater. Today Commun. 25 (2020) 101292. https://doi.org/10.1016/j.mtcomm.2020.101292.

[7] J. Du, M. Strangwood, C.L. Davis, J. Mater. Sci. Technol. 28 (2012) 878–888. https://doi.org/10.1016/S1005-0302(12)60146-7.

[8] T. Shang, W. Wang, J. Kang, S. Luo, M. Zhu, J. Mater. Res. Technol. 24 (2023) 3608–3627. https://doi.org/10.1016/j.jmrt.2023.03.155.

[9] L. Xing, M. Wang, J. Guo, Z. Zhang, F. Zeng, B. Chen, Y. Bao, Metals 9 (2019) 1269. https://doi.org/10.3390/met9121269.

[10] M. Prikryl, A. Kroupa, G.C. Weatherly, S.V. Subramanian, Metall. Mater. Trans. A 27 (1996) 1149–1165. https://doi.org/10.1007/BF02649854.

[11] D.P. Zhan, H.Z. Jiang, W. Gong, J.C. He, Chin. J. Proc. Eng. 9 (2009) 238–241. https://doi.org/10.3321/j.issn:1009-606X.2009.z1.051.

[12] T. Liu, D. Chen, M. Long, P. Liu, H. Duan, L. Gui, H. Fan, H. Chen, Met. Sci. Heat Treat. 61 (2020) 534–542. https://doi.org/10.1007/s11041-020-00477-5.

[13] L. Gui, M. Long, H. Zhang, D. Chen, S. Liu, Q. Wang, H. Duan, J. Mater. Res. Technol. 9 (2020) 5499–5514. https://doi.org/10.1016/j.jmrt.2020.03.075.

[14] W. Liang, R. Wu, Q. Yuan, J. Hu, Trans. Indian Inst. Met. 73 (2020) 151–159. https://doi.org/10.1007/s12666-019-01816-8.

[15] N. Li, L. Wang, Z.L. Xue, C.Z. Li, A. Huang, F.F. Wang, Results Phys. 16 (2020) 102929. https://doi.org/10.1016/j.rinp.2020.102929.

[16] X.L. Li, S.D. Wang, X.T. Deng, Y.J. Zhang, C.S. Cheng, G.D. Wang, Acta Metall. Sin. 51 (2015) 784–790. https://doi.org/10.11900/0412.1961.2014.00606.

[17] H. Goto, K.I. Miyazawa, K.I. Yamaguchi, S. Ogibayashi, K. Tanaka, ISIJ Int. 34 (1994) 414–419. https://doi.org/10.2355/tetsutohagane1955.79.9_1082.

[18] K. Oikawa, H. Ohtani, K. Ishida, T. Nishizawa, ISIJ Int. 35 (1995) 402–408. https://doi.org/10.2355/ISIJINTERNATIONAL.35.402.

[19] M.T. Nagata, J.G. Speer, D.K. Matlock, Metall. Mater. Trans. A 33 (2002) 3099–3110. https://doi.org/10.1007/s11661-002-0294-z.

[20] H. Yu, Y.L. Kang, Z.Z. Zhao, H. Sun, J. Iron Steel Res. Int. 13 (2006) No. 5, 30–36. https://doi.org/10.1016/S1006-706X(06)60091-5.

[21] B.L. Bramfitt, Metall. Trans. 1 (1970) 1987–1995. https://doi.org/10.1007/BF02642799.

[22] M. Wang, Y.P. Bao, H. Cui, H.J. Wu, W.S. Wu, J. Iron Steel Res. 22 (2010) No. 7, 29–32. https://doi.org/10.13228/j.boyuan.issn1001-0963.2010.07.008.

[23] Q.R. Tian, D.L. Cheng, G.C. Wang, J. Iron Steel Res. 30 (2018) 857–865. https://doi.org/10.13228/j.boyuan.issn1001-0963.20180094.

[24] J.L. Qiao, F.H. Guo, J.W. Hu, S.T. Qiu, X.Z. Zhang, Trans. Mater. Heat Treat. 42 (2021) 110–118. https://doi.org/10.13289/j.issn.1009-6264.2020-0267.

[25] B. Lu, Y. Li, H. Wang, Y. Wang, W. Yu, Z. Wang, G. Xu, J. Mater. Res. Technol. 22 (2023) 2532–2548. https://doi.org/10.1016/j.jmrt.2022.12.082.

[26] Z. Ma, D. Janke, ISIJ Int. 38 (1998) 46–52. https://doi.org/10.2355/isijinternational.38.46.

[27] J. Fu, J. Zhu, L. Di, D.L. Liu, Y.L. Wang, Acta Metall. Sin. 36 (2000) 801–804. https://doi.org/10.3321/j.issn:0412-1961.2000.08.00.

[28] J.X. Chen, Data manual for charts commonly used in steelmaking (Version 2), Metallurgical Industry Press, Beijing, China, 2010.

[29] X.H. Huang, Principles of iron and steel metallurgy (Version 4), Metallurgical Industry Press, Beijing, China, 2013.

[30] I. Ohnaka, ISIJ Int. 26 (1986) 1045–1051. https://doi.org/10.2355/isijinternational.26.1045.

[31] W.Y. Su, R.L. Zhang, B. Shao, Int. J. Min. Mater. 11 (2002) 105–108. https://doi.org/10.3969/j.issn.1004-0579.2002.01.024.

[32] Q.L. Yong, The second phase in steel materials, Metallurgical Industry Press, Beijing, China, 2010.

[33] Z. Shi, X. Chai, F. Chai, H. Su, T. Pan, Q. Wang, R. Wang, C. Yang, Mater. Lett. 175 (2016) 266–270. https://doi.org/10.1016/j.matlet.2016.04.033.

[34] Y. Wan, Q.W. Chen, Heat Treat. Met. 38 (2013) No. 11, 63–66. https://doi.org/10.13251/j.issn.0254-6051.2013.11.021.